

Research Article

Influence of Different Grouting Parameters on Mechanical and Strain Energy Characteristics of Different-Length Fractured Limestone in a Coalfield North of Yellow River: A Numerical Study Based on Particle Flow Code

Hao Li,^{1,2} Juntao Chen ,^{1,3} Qing Ma ,^{1,4} Dongxiu Jia,⁵ Binbin Cheng,⁶ Ziqun Fu,¹ Lei Liu,⁵ Hongyun Guo,⁵ Zhu Qu,⁷ and Jingping He⁵

¹College of Energy and Mining Engineering, Shandong University of Science and Technology, Qingdao 266590, China

²Geotechnical and Structural Engineering Research Center, Shandong University, Jinan 250061, China

³State Key Laboratory of Coal Mining and Clean Utilization, Beijing 100013, China

⁴State Key Laboratory of Hydrosience and Engineering, Tsinghua University, Beijing 100084, China

⁵Qiuji Coal Mine, Shandong Energy Xinwen Mining Group Co., Ltd., Dezhou 251105, China

⁶China Center for Safety Research, MEM, Beijing 100713, China

⁷Jining Energy Development Group Corporation Ltd., Jining 272400, China

Correspondence should be addressed to Juntao Chen; chenjuntao@sdust.edu.cn and Qing Ma; qingma819@126.com

Received 8 September 2022; Revised 20 October 2022; Accepted 24 November 2022; Published 3 March 2023

Academic Editor: Zhengzheng Xie

Copyright © 2023 Hao Li et al. This is an open access article distributed under the Creative Commons Attribution License, which permits unrestricted use, distribution, and reproduction in any medium, provided the original work is properly cited.

Floor grouting reinforcement and aquifer reform can effectively improve the water barrier performance of fractured rock mass, which is widely used to prevent water inrush from a confined aquifer in the Clean Utilization and SDUST Research Fund floor. In order to reveal the mechanical and strain energy characteristics of fractured rock mass after grouting with different grouting parameters, the discrete element numerical simulation software PFC is used to study the mechanical and strain energy characteristics of limestone after filling the fractures with cement stones with different parameters. The numerical test results show that the displacement of the limestone grouting stone bodies with a longer prefabricated crack length decreases more obviously after grouting, and the strain energy, dissipation energy, and total input energy increase when the strengthened limestone sample is destroyed. The greater the stiffness of the cement stone, the easier the limestone grouting stone bodies will be destroyed from the position of the prefabricated crack. The internal friction angle of cement stones has little effect on the strength, deformation, and energy characteristics of limestone. Under the same cohesion, the number and the distribution range of secondary cracks of limestone grouting stone bodies with smaller prefabricated crack length are larger. However, with the increase of the tensile strength of the cement stones, the number, distribution range, and strength of the secondary fractures of the limestone grouting stone bodies are increasing. The longer the prefabricated crack is, the greater the influence of grouting parameters on the rock. The study provides a reference for the selection of reinforcement material parameters during grouting reinforcement.

1. Introduction

Rock grouting reinforcement is an important means to prevent water inrush, collapse, and other accidents in mines. The research on the mechanical properties of the rock mass after grouting reinforcement has important scientific signif-

icance for the design and maintenance of rock mass projects such as mines and tunnels [1–3]. Grouting reinforcement can not only change the stress structure of rock engineering from the macroperspective but also improve the cracks and holes from the microperspective. In this way, the strength of the rock mass and the stability of the project can be

improved. However, it is necessary to study the failure mechanism of the rock mass after grouting reinforcement [4–6]. This is of great significance to the stability of grouting rock engineering.

In order to reveal the influence of grouting on the mechanical characteristics of fractured rock, domestic and foreign scholars have conducted a lot of research on it through indoor tests and numerical simulation [7, 8] and further studied the mechanism of grouting reinforcement on this basis [9–13]. Yang [14] studied the structure of randomly fractured rock mass, the law of grouting permeability, the characteristics of randomness and anisotropy, and the stability of grouting reinforcement. An analysis model of grouting seepage and stability of roadway surrounding rock after reinforcement was established. Liu et al. [15] compared the closure strength and shear strength of the crack surface of the rock mass before and after grouting reinforcement and obtained the change rule of the mechanical properties of the rock mass crack before and after grouting. Wang et al. [16, 17] analyzed the influence of grouting strength and bonding force on the grouting reinforcement effect through static and dynamic mechanical tests of rock mass after grouting reinforcement. It reveals the nonlinear change mechanism of the energy carried by the rock and its life. The double logarithm fatigue life equation of the fractured rock after grouting reinforcement is established. Wang et al. [16] analyzed the influence of the number and position of cracks on the strength of grouting stone bodies through the independently designed sample preparation method of crack samples. Wang et al. [17] analyzed the stress-strain relationship and mechanical characteristics of diabase fissure grouting under different fracture geometries by conducting uniaxial and conventional triaxial compression tests on diabase original rock and its fissure grouting stone bodies. Wang et al. [18–20] established a variety of defective coal rock samples by using PFC2D software considering the different dip angles of fractures and positions of cavities. The stress-strain characteristics, crack evolution, and acoustic emission (AE) characteristics of coal with different cracks and holes are discussed. Based on the AE characteristics, the damage evolution law of rock materials with defects is studied [20–25]. From the above research, it can be found that the research on the mechanical properties of the rock mass after grouting reinforcement mainly focuses on the types of grouting materials and the strength after grouting. At present, the research on the influence of grouting parameters on the mechanical properties and energy characteristics of rock after grouting reinforcement has not been systematically published. The failure mechanism after grouting reinforcement has not formed a perfect explanation. In-depth understanding of the mechanical characteristics of the rock after grouting reinforcement with different grouting parameters can not only have an important impact on the selection of grouting materials but also have an impact on the overall safety of the rock project after reinforcement.

On the basis of the above research, this paper establishes limestone grouting stone body samples with different angles of fractures and uses the fish program to program the fractures for grouting reinforcement. Through the uniaxial

compression test, the effects of the crack angle and micro-parameters of grouting reinforcement material (stiffness, internal friction angle, cohesion, and tensile strength, respectively, represent the rigidity, internal friction angle, contact cohesion, and tensile strength of particles) on limestone mechanics and strain energy characteristics are studied. The paper reveals the failure mechanism of limestone reinforcement, which provides a reference for the selection of grouting reinforcement material parameters.

2. Numerical Model and Test Scheme

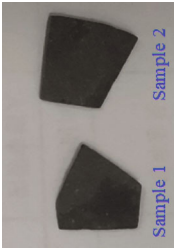
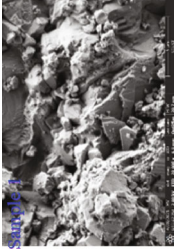
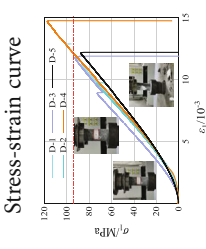

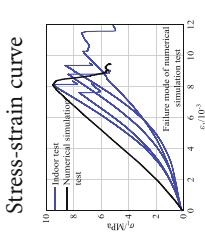
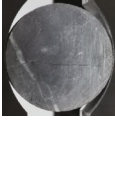
2.1. Raw Data Acquisition. Electron microscope scanning, uniaxial compression, and Brazilian splitting tests were carried out. On the one hand, the basic physical and mechanical parameters of limestone porosity and elastic modulus can be obtained; on the other hand, it can be used to compare the follow-up test data of fractured limestone and grouted limestone. The test results are shown in Table 1. The study of the grouting and reinforcement characteristics of fractured limestone is more systematic (all sample standards and test specifications are carried out in strict accordance with the *Rock Test Regulations for Water Conservancy and Hydropower Engineering* (SL/T 264-2020) [26]).

2.2. Parameter Calibration and Test Scheme. When using particle flow simulation software to carry out research, it is necessary to substitute the microscopic physical and mechanical parameters and bond properties of particles into the model. However, these parameters are not simply substituted into the model with the physical and mechanical parameters of limestone obtained above [27, 28]. Therefore, before carrying out the numerical simulation test, the model needs to be calibrated. The general process is as follows: (1) A 1:1 numerical model is established according to the laboratory test state. (2) Based on the macro-meso-transformation method, the physical and mechanical parameters of limestone obtained in laboratory tests were substituted into the mesomechanical parameters used in the model. (3) Calculate and solve. The calculation and calibration principle of the parallel bond model of the PFC model (version 5.0) is shown in Figures 1 and 2.

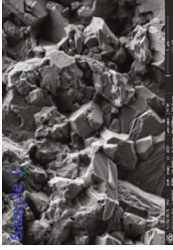
2.3. Test Calibration and Parameter Checking of Limestone. Based on the laboratory experiments to obtain mechanical parameters of limestone, literature [29] outlines the steps of the mesoscopic mechanics parameter calibration method of limestone, mesoscopic parameter calibration, and granular flow test, to obtain the required mesoscopic mechanics parameters, as follows.

- (1) A numerical model with a height of 100 mm and a diameter of 50 mm was established according to the size of the uniaxial test model
- (2) Literature [29] shows that if the ratio between the shortest edge of the model and the average particle radius is greater than 40, and the number of particles on the shortest edge of the model is greater than 30, the calculation efficiency can be improved as far as

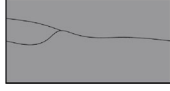
TABLE 1: Limestone parameter acquisition tests.

| Test names | Test content | | Test data |
|----------------------------|--|---|---|
| SEM analysis tests |  |  | Compact structure |
| Uniaxial compression tests |  |  | Average uniaxial compressive strength = 94.52 MPa Average elastic modulus = 9.36 GPa |
| Brazilian splitting tests |  |  | Average tensile strength = 9.27 MPa Average ratio of tension and compression = 0.098 |

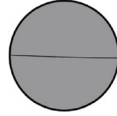
Micromorphological features and mineral components



Damage sample sketch



Damage sample sketch



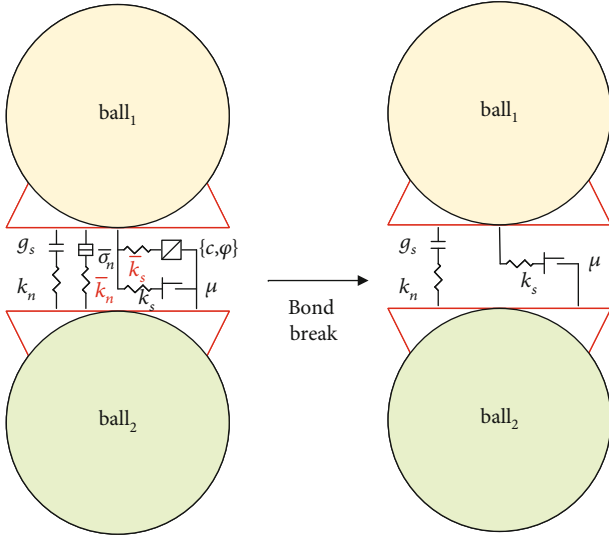


FIGURE 1: Linear parallel bond mode.

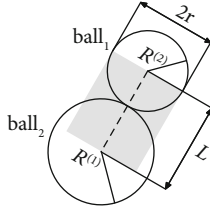


FIGURE 2: Linear parallel bond contact of ball-ball.

possible on the premise of ensuring the calculation accuracy of the model. Based on the results of this study, the particle size distribution can be determined

- (3) Based on the indoor test of the limestone for Poisson's ratio, elastic modulus, uniaxial compressive strength and uniaxial tensile strength, porosity, density, cohesion, and internal friction angle, the transformation for mesoscopic parameters stiffness ratio, stiffness, cohesion, tensile strength, porosity, density, cohesion, and internal friction angle, after the transformation parameters, are shown in Table 2
- (4) The uniaxial compression and Brazil splitting simulation tests were carried out to verify the data accuracy

Figure 3 shows the $\sigma_1 - \varepsilon_1$ curve of the laboratory test, which is the $\sigma_1 - \varepsilon_1$ curve of the simulation test and failure pattern of uniaxial compression. As can be seen from Figure 3, the numerical simulation $\sigma_1 - \varepsilon_1$ curve is in good agreement with the laboratory test results. The average compressive strength was 94.52 MPa, the average elastic modulus was 9.36 GPa, and the average peak strain was 1.18. The corresponding numerical simulated compressive strength is 98.15 MPa (error value is 3.84%), elastic modulus is 9.64 GPa (error value is 2.99%), and the peak strain is 1.06 (error value is 10.17%). It can be found that the elastic modulus and compressive strength are very close except for the large strain difference. Because of the defects of the simula-

tion software itself, it cannot completely simulate all the deformation stages of the rock. The indoor test results show obvious stages of pore and fissure compaction, and the software modeling needs to go through three stages: particle generation, particle balance, and cementation. In the particle balance stage, the particle distribution has been densified to the greatest extent, so it is difficult to simulate the pore and fissure compaction stage of the rock; thus, the simulated strain will be smaller than the indoor test to a certain extent.

Figure 4 shows the $\sigma_1 - \varepsilon_1$ curve of the Brazilian splitting numerical simulation laboratory test, which is the $\sigma_1 - \varepsilon_1$ curve of the simulation test and the failure pattern. As can be seen from the figure, the numerical simulation $\sigma_1 - \varepsilon_1$ curve is in good agreement with the laboratory test results. The average tensile strength obtained from the laboratory test is 9.27 MPa, and the corresponding numerical simulated compressive strength is 9.51 MPa (error value is 2.59%). It can be found that the tensile strength is also very close, but due to the defects of the simulation software itself, it cannot completely simulate all deformation stages of the rock. Both indoor experiment results show the apparent ore fissure compaction stage, and the software modeling needs to reflect the three stages of particle generation, particle balance, and cementation; the particle balance stage has a maximum particle distribution density, so it is difficult to simulate the rock pore fissure compaction stage, and the strain of the simulation test is less than that of the indoor test to some extent. At the same time, the intensity will be higher than the laboratory test to some extent. The failure mode of the numerical simulation limestone model is basically consistent with that of the laboratory experiment in Brazil.

The reliability of the parameters is verified via uniaxial compression and the Brazil splitting test, which proves that it is feasible to use the parameters to study the grouting mechanism of floor limestone in the Yellow River north coal mine.

2.4. Numerical Simulation Schemes. On the basis of the limestone mechanical parameters above the parameter calibration of the experiment and simulation, the limestone aquifer parameters obtained with the Yellow River north coalfield floor numerical calculation model are basically identical; on the basis of this model, with limestone precast with 10, 30, and 50 mm cracks, the effects of the changes of cement stones' stiffness, internal friction angle, cohesion, and tensile strength on the strength, deformation characteristics, and crack evolution of limestone grouting stone bodies when 10, 30, and 50 mm cracks are prefabricated in limestone are studied:

- (1) The internal friction angle, cohesion, and tensile strength of stone bodies were unchanged, and the stiffness changes were 0.1, 0.5, 1.0, 1.5, 2.0, 2.5, and 3.0 GPa
- (2) The stiffness, cohesion, and tensile strength of stone bodies remained unchanged, and the internal friction angle changed to 10, 15, 30, 45, 60, 75, and 89°
- (3) The stiffness, internal friction angle, and bonding tensile strength of stone bodies remained unchanged,

TABLE 2: Mesoparameters of limestone.

| k -ratio | E_{mod} (GPa) | Pb_k -ratio | Pb_e_{mod} (GPa) | Pb_ten (MPa) | Pb_coh (MPa) | Porosity | Density (kg/m ³) | Pb_fa (°) |
|------------|-----------------|----------------|---------------------|-----------------|-----------------|----------|------------------------------|--------------|
| 5.72 | 5.24 | 5.72 | 5.24 | 72.56 | 10.24 | 2.23 | 2.66 | 53 |

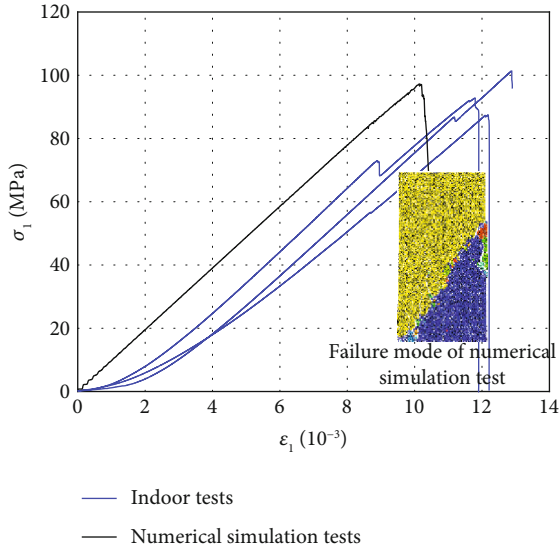


FIGURE 3: Curve of $\sigma_1 - \epsilon_1$ laboratory test, curve of $\sigma_1 - \epsilon_1$ simulation test and failure mode (uniaxial compression).

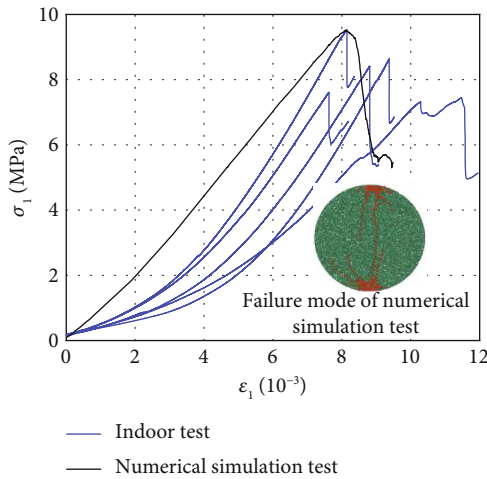


FIGURE 4: Curve of $\sigma_1 - \epsilon_1$ laboratory test, curve of $\sigma_1 - \epsilon_1$ simulation test and failure mode (Brazil splitting).

while the cohesion of stone bodies changed to 1.0, 5.0, 1.0, 1.5, 2.0, 2.5, and 3.0 MPa

- (4) The stiffness, internal friction angle, and bond cohesion of stone bodies remained unchanged, while the bond tensile strength changed to 1.0, 5.0, 1.0, 1.5, 2.0, 2.5, and 3.0 MPa

3. Results and Discussion

3.1. Failure Law of Limestone and Grouting Reinforcement Bodies. When there are 10 mm, 30 mm, and 50 mm cracks preformed, the variation law of limestone internal displacement is shown in Figure 5 (in the crack model, the front picture is the model without grouting and the rear picture is the model after grouting; the same below). From left to right, they are limestone, limestone preformed fractured limestone, and limestone grouting stone bodies. In order to eliminate the differences between the tests as far as possible, on the premise of ensuring the same calculation step length, the displacement distribution maps were all limestone calculated for 10,000 steps and then intercepted. As can be seen from Figure 5, the limestone without cracks has a uniform distribution of displacement, with large displacement up and down and small displacement in the middle of the limestone. However, in the precast fissure limestone, the displacement has a great difference around the fissure. The maximum displacements around the prefabricated 10, 30, and 50 mm cracks were 2.0×10^{-5} , 3.5×10^{-5} , and 5×10^{-5} m, respectively, and the minimum values were 1.62×10^{-6} , 1×10^{-5} , and 1.5×10^{-5} m, respectively. The difference values are 5.0×10^{-6} m, 2.5×10^{-5} m, and 3.5×10^{-5} m, respectively. That is, with the increase of the prefabricated fracture length, the concentration degree of displacement around the fracture increases, and the difference of displacement becomes larger and larger. After grouting reinforcement, the difference of displacement distribution around the limestone fissure is reduced. The maximum displacement around the grouting stone body fissure with 10, 30, and 50 mm fissures is 5.0×10^{-6} , 1.5×10^{-5} , and 2.5×10^{-5} m, respectively. The minimum values were 1.62×10^{-6} , 1.62×10^{-6} , and 1.62×10^{-6} m, and the differences were 3.38×10^{-6} , 1.34×10^{-5} , and 2.34×10^{-5} m, respectively. After grouting reinforcement, the maximum displacement around the prefabricated 10, 30, and 50 mm cracks of grouting stone body limestone decreases by 1.5×10^{-5} m, 2×10^{-5} m, and 2.5×10^{-5} m, respectively. It can be concluded that, after the grouting reinforcement of the fractured rock mass, the concentration degree of limestone displacement around the fracture decreases, which shows that the maximum displacement around the fracture decreases, and the difference value of displacement decreases. And with the increase of the length of the fracture, the maximum displacement around the limestone fracture decreases, and the difference value of displacement decreases.

When there are prefabricated cracks of 10 mm, 30 mm, and 50 mm, the distribution law of cracks in limestone failure is shown in Figure 6. From left to right, they are limestone, prefabricated cracked limestone, and limestone grouting stone bodies. The energy index values of each

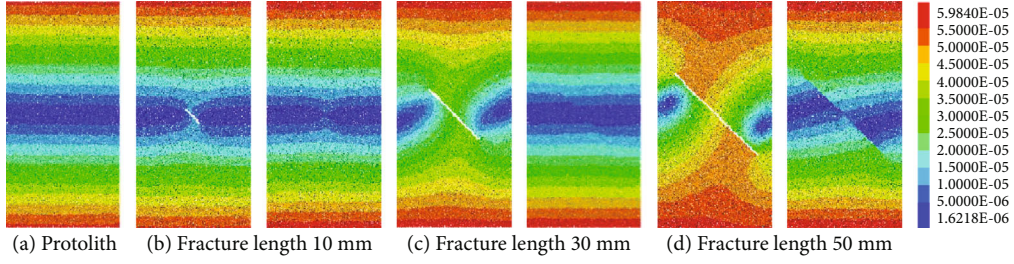


FIGURE 5: Displacement change in limestones with different prefabricated crack lengths.

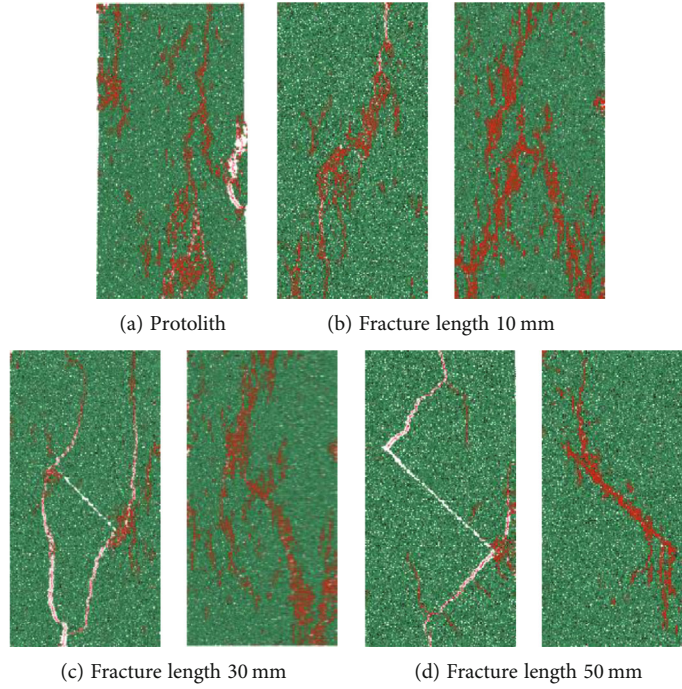


FIGURE 6: Crack distribution in the limestones with different prefabricated crack lengths.

specimen in simulation tests derived from Equations (1) and ((2)) [30] are shown in Table 3. The existence of prefabricated fractures leads to the inconsistency of limestone fracture evolution; that is, the cracks generated by loading start from the end of the prefabricated fractures and develop until they reach the boundary of the limestone model, where macroscopic fracture surfaces appear and the limestone is destroyed. With the increase of fracture length, the distribution of fractures is significantly more concentrated and the number of fractures is less. According to the calculation of Equations (1) and ((2)) [30], the rock absorbs less energy and will be damaged. Therefore, it can be concluded that the shorter the length of prefabricated fractures is, the more fractures will be produced when limestone is destroyed. The shorter the prefabricated fractures are, the more energy will be absorbed to cause limestone to fail, and the strength of limestone is higher. The longer the length of prefabricated fracture is, the fewer the number of fractures will be generated when limestone is destroyed, and the longer the prefabricated fracture needs to absorb less energy to cause limestone to fail and the strength of limestone is low. After

grouting reinforcement, the number of cracks in limestone is obviously higher than that before grouting reinforcement, and the total absorbed energy density, elastic energy density, and dissipated energy density all increase to a certain extent. With the increase of the length of the prefabricated fracture, the increase of the total energy density, elastic energy density, and dissipated energy density of limestone before grouting also increases; it shows that limestone with long prefabricated cracks is more significantly affected by grouting.

$$U_0 = U_1 + U_3, \quad (1)$$

$$U_1 = \frac{\sigma_1^2}{2E}, \quad (2)$$

where U_0 is the total energy density absorbed by the rock, kJ/m^3 , which is obtained by integrating the stress-strain curve; U_1 is the elastic energy density, kJ/m^3 ; and U_3 is the dissipated energy density, kJ/m^3 .

TABLE 3: Energy index value of each specimen in simulation tests.

| Specimen type | Crack length (mm) | Compressive strength (MPa) | Postpeak intensity 70% points | | |
|-------------------------------|-------------------|----------------------------|---|---|--|
| | | | Energy density of absorption (KJ/m ³) | Elastic energy density (KJ/m ³) | Dissipated energy density (KJ/m ³) |
| Protolith | | 98.15 | 633.94 | 198.21 | 435.73 |
| Prefabricated crack | 10 | 69.14 | 343.43 | 158.02 | 185.41 |
| | 30 | 43.37 | 225.94 | 91.50 | 134.44 |
| | 50 | 23.86 | 108.25 | 33.49 | 74.76 |
| Grouting reinforcement bodies | 10 | 91.50 | 597.36 | 190.17 | 407.19 |
| | 30 | 65.86 | 290.87 | 91.74 | 199.13 |
| | 50 | 37.46 | 253.15 | 80.94 | 172.21 |

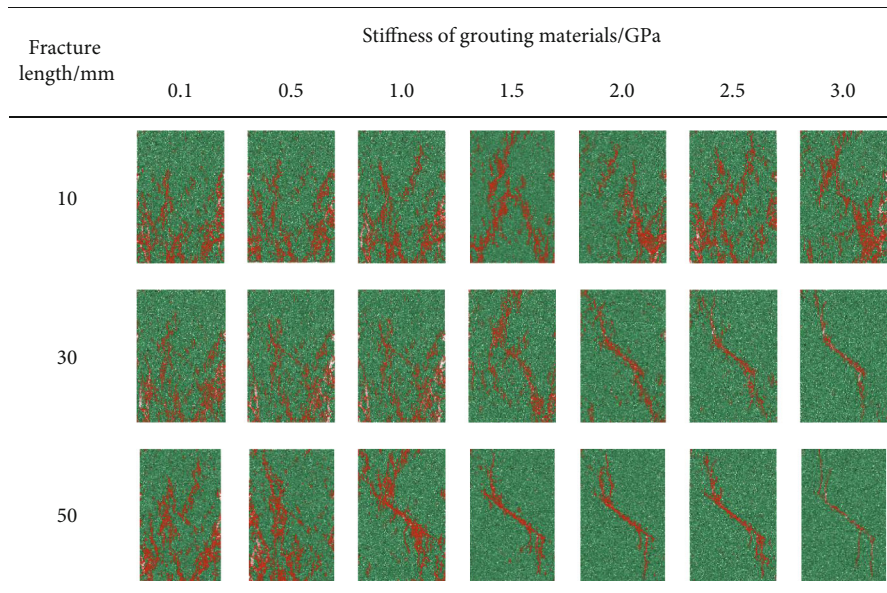


FIGURE 7: Crack distribution of limestone grouting reinforcement bodies under different crack lengths and different stiffness values of grouting stone bodies.

3.2. *Influence Law of Stiffness.* It can be seen from Figure 7 (the same length of crack corresponds to 7 different stiffness values, which are 0.1, 0.5, 1.0, 1.5, 2.0, 2.5, and 3.0 GPa in order) that, with the increase of limestone grouting concrete body stiffness, the distribution of the secondary fracture is gradually concentrated; with regard to the stiffness value, the smaller the scattered secondary fracture distribution, the bigger the stiffness value; the secondary cracks are gradually shown to start development at the prefabricated crack tip until the limestone model boundaries, where the law of the limestone damage appears to stop, when the crack length is larger. The rule is even more pronounced. Therefore, it can be concluded that the stiffness change of limestone stone bodies will affect the generation and expansion of limestone secondary cracks. The greater the stiffness of the limestone grouting rock mass, the more concentrated the distribution of cracks in the limestone grouting bodies, and it is easier to result in damage around the prefabricated cracks in the limestone grouting bodies.

As can be seen from Figure 8, the grouting stone bodies' uniaxial compressive strength of limestone prefabricated with 10, 30, and 50 mm cracks decreases with the increase of cement stones stiffness. When the stiffness of the cement stones increased from 0.1 GPa to 3.0 GPa, the uniaxial compressive strength of limestone grouting stone bodies with 10 mm cracks decreased from 93.71 MPa to 92.30 MPa. The uniaxial compressive strength of limestone grouting bodies with 30 mm crack decreased from 93.28 MPa to 70.01 MPa, and the uniaxial compressive strength of limestone grouting bodies with 50 mm crack decreased from 82.48 MPa to 51.15 MPa.

As can be seen in Figure 9, the peak strain variables of limestone grouting stone bodies preformed with 10, 30, and 50 mm cracks all decreased with the increase of stone body stiffness. When the stiffness of the cement stones increases from 0.1 GPa to 3.0 GPa, the peak strain of the limestone grouting stone bodies with 10 mm cracks decreases from 12.56×10^{-3} to 12.35×10^{-3} . The peak strain

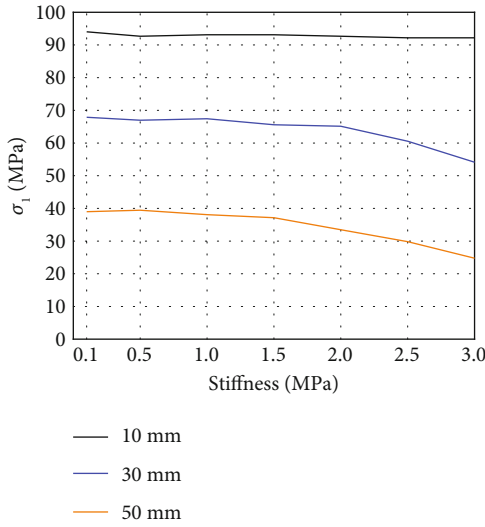


FIGURE 8: Uniaxial compressive strength of limestone grouting reinforcement bodies under different crack lengths and different stiffness values of grouting stone bodies.

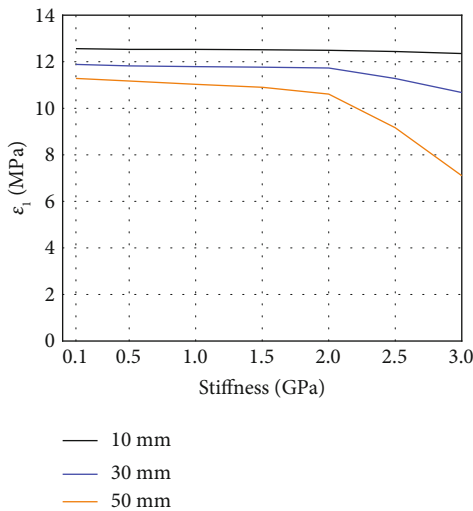


FIGURE 9: Peak strain of limestone grouting reinforcement bodies under different crack lengths and different stiffness values of grouting stone bodies.

of limestone grouting with 30 mm crack decreased from 11.88×10^{-3} to 10.68×10^{-3} , and the peak strain of limestone grouting with 50 mm crack decreased from 11.28×10^{-3} to 7.10×10^{-3} .

To sum up, the rigidity of cement stone in limestone grouting increases, which will weaken the grouting reinforcement effect; longer crack length of limestone grouting stone bodies is affected by the larger stiffness of the cement stones; use of the slurry grouting that can form cement stones with large stiffness not only reduces the strength but also reduces the deformation resistance compared with the slurry grouting that can form cement stones with small stiffness.

3.3. Influence Law of Internal Friction Angle. Other parameters such as stiffness, cohesion, and tensile strength were not changed, and the internal friction angle values of the cement stones were changed to 1, 15, 30, 45, 60, 75, and 89°. The mechanical properties, crack expansion process, and fracture characteristics of limestone grouting stone bodies were observed. Through the test, it is found that the change of internal friction angle of the cement stones has no effect on the limestone grouting stone bodies with 10, 30, and 50 mm cracks.

3.4. Influence Law of Bonding Cohesion. It can be seen from Figure 10 (cracks with the same length correspond to 7 different cohesive values, which are 0.1, 0.5, 1.0, 1.5, 2.0, 2.5, and 3.0 MPa in order) that the change of cohesion of cement stones has little effect on the evolution and distribution of the main limestone cracks. Comparing the grouting stone bodies of limestone with different preformed crack lengths under the same cohesion, the number of secondary cracks is larger and the distribution range is larger when the preformed crack length is smaller. When the preformed crack length is larger, the distribution of secondary cracks is more concentrated and the number of cracks is less.

It can be seen from Figure 11 that when the preformed crack length is small (=10 mm), the uniaxial compressive strength of limestone grouting stone bodies decreases with the increase of the cohesion of cement stones, but the overall change range is small (92.94–91.87 MPa). The uniaxial compressive strength of limestone grouting stone bodies increases with the increase of cohesion of cement stones when the preformed crack length is larger (>10 mm). The cohesion of grouting cement stones increased from 0.1 MPa to 3.0 MPa, and the uniaxial compressive strength of the limestone grouting stone bodies with 30 mm preformed cracks increased from 59.55 MPa to 85.54 MPa, with an increase of 25.99 MPa. The uniaxial compressive strength of limestone grouting stone bodies with 50 mm preformed cracks increased from 30.32 MPa to 59.10 MPa, an increase of 28.78 MPa.

As can be seen from Figure 12, the prefabricated crack length is small (=10 mm). The peak strain of limestone grouting rock mass decreases with the increase of the cohesion of cement stones, but the overall reduction is smaller ($12.44 \times 10^{-3} \sim 12.60 \times 10^{-3}$). The uniaxial compressive strength of limestone grouting stone bodies increases with the increase of cohesion of cement stones when the preformed crack length is larger (>10 mm). When the cohesion of cement stones increased from 0.1 MPa to 3.0 MPa, the peak strain of limestone grouting stone bodies with 30 mm cracks increased from 5.94×10^{-3} to 7.97×10^{-3} , with an increase of 2.03×10^{-3} . The peak strain of limestone grouting stone bodies with 50 mm cracks increased from 3.30×10^{-3} to 5.52×10^{-3} , with an increase of 2.22×10^{-3} .

In conclusion, with the increase of cohesion of cement stones, the strength and deformation of limestone grouting stone bodies with small preformed cracks (=10) are almost not affected. After grouting, the strength and deformation of limestone grouting stone bodies with large prefabricated cracks (>10) change more. The longer the precast crack is,

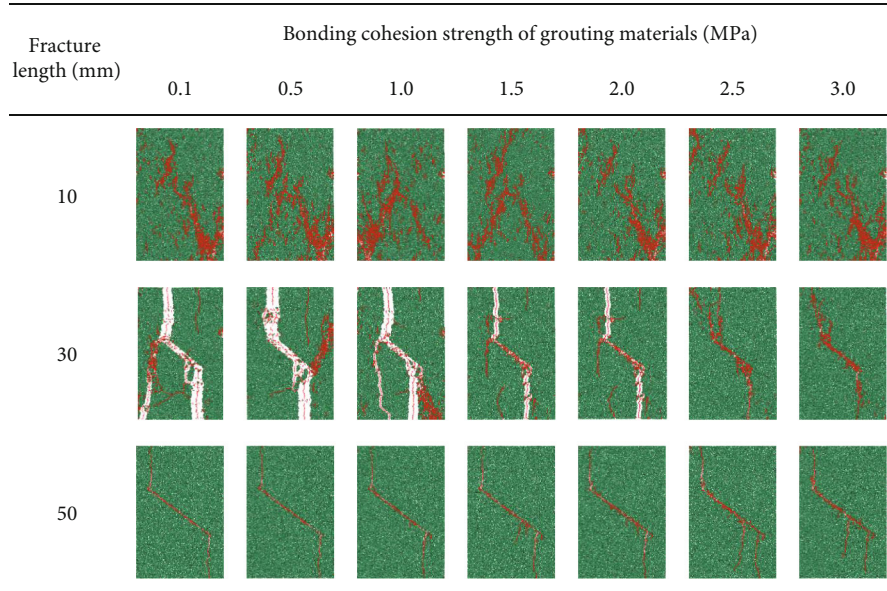


FIGURE 10: Crack distribution of limestone grouting reinforcement bodies under different crack lengths and different bonding cohesion values of grouting stone bodies.

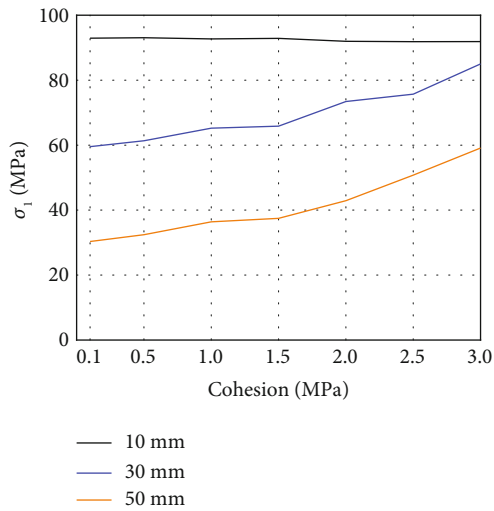


FIGURE 11: Uniaxial compressive strength of limestone grouting reinforcement bodies under different crack lengths and different bonding cohesion values of grouting stone bodies.

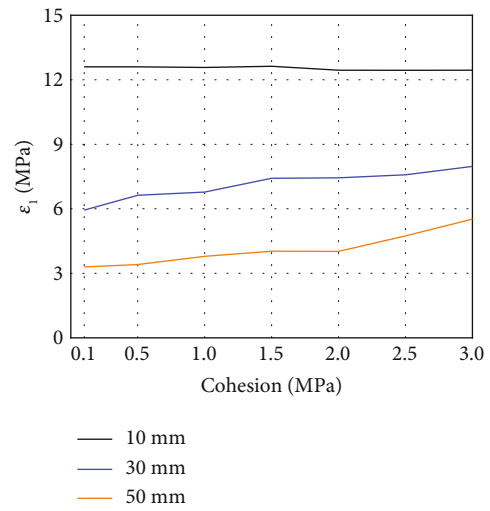


FIGURE 12: Peak strain of limestone grouting reinforcement bodies under different crack lengths and different bonding cohesion values of grouting stone bodies.

the greater the influence of cement stones' cohesion on the strength and deformation of limestone grouting rock mass.

3.5. Influence Law of Bonding Tensile Strength. It can be seen from Figure 13 (cracks with the same length correspond to 7 different tensile strength values, which are 0.1, 0.5, 1.0, 1.5, 2.0, 2.5, and 3.0 MPa in order) that when the tensile strength of cement stones is small, the distribution of secondary cracks mostly starts from the preformed cracks and ends at the limestone grouting stone bodies' boundary. With the increase of tensile strength of bonding, the distribution range of secondary cracks expands. Compared with limestone grouting stone bodies with different prefabricated

crack lengths under the same cement stones' tensile strength, when the prefabricated crack length is small, the number of secondary cracks is small and the distribution range is concentrated, which starts from the prefabricated crack tip and ends at the grouting stone bodies' boundary. When the preformed crack length is large, the distribution of secondary cracks is more scattered and the number of cracks is more.

It can be seen from Figure 14 that when the length of prefabricated crack is small (=10 mm), the uniaxial compressive strength of limestone grouting stone bodies fluctuates with the change of tensile strength of cement stones but generally fluctuates in the range of 88.49~92.25 MPa, with a small fluctuation range. The uniaxial compressive strength

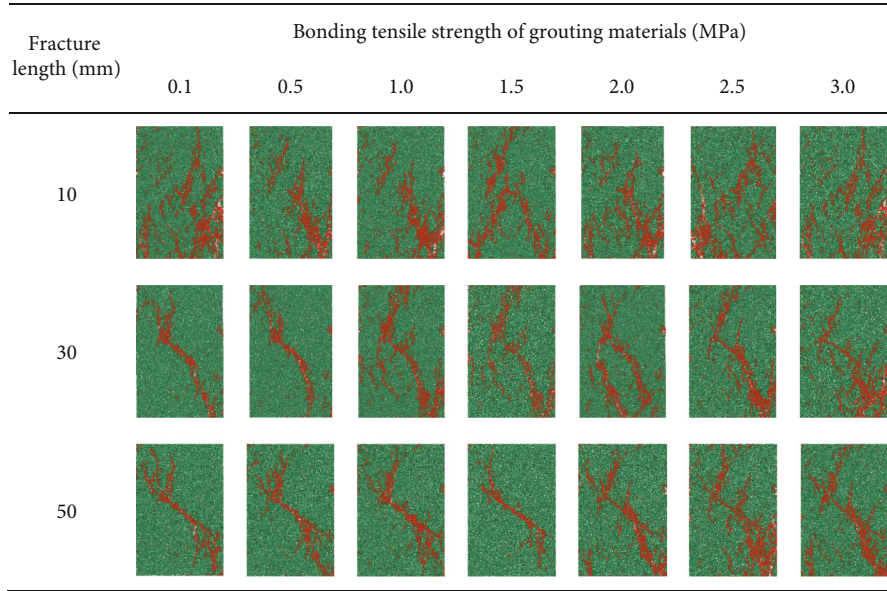


FIGURE 13: Crack distribution of limestone grouting reinforcement bodies under different crack lengths and different bonding tensile strength values of grouting stone bodies.

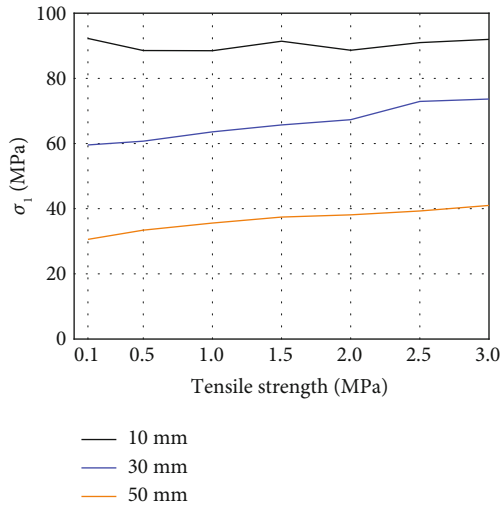


FIGURE 14: Uniaxial compressive strength of limestone grouting reinforcement bodies under different crack lengths and different bonding tensile strength values of grouting stone bodies.

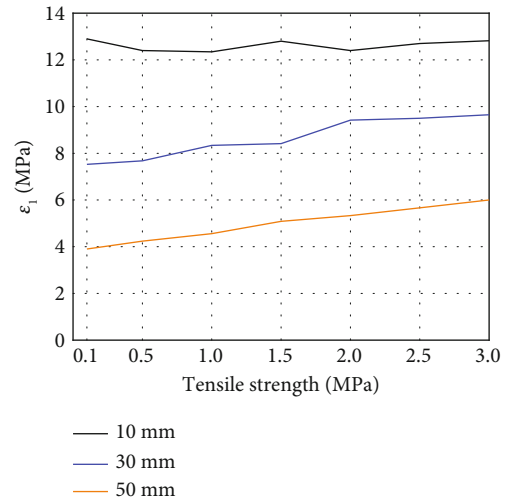


FIGURE 15: Peak strain of limestone grouting reinforcement bodies under different crack lengths and different bonding tensile strength values of grouting stone bodies.

of limestone grouting stone bodies increases with the increase of tensile strength of cement stones when the preformed crack length is larger (>10 mm). The tensile strength of cement stones increased from 0.1 MPa to 3.0 MPa, and the uniaxial compressive strength of limestone grouting stone bodies with 30 mm preformed cracks increased from 59.57 MPa to 73.67 MPa, with an increase of 14.10 MPa; the peak strain of limestone with 50 mm preformed cracks increased from 30.59 MPa to 41.00 MPa, an increase of 10.41 MPa.

It can be seen from Figure 15 that when the length of prefabricated crack is small ($=10$ mm), the peak strain of

limestone grouting stone bodies fluctuates with the change of tensile strength of cement stones but generally fluctuates in the range of 12.45×10^{-3} to 12.92×10^{-3} , with a small fluctuation range. When the preformed crack length is larger (>10 mm), the peak strain of limestone grouting stone bodies increases with the increase of tensile strength of cement stones. When the tensile strength of cement stones increased from 0.1 MPa to 3.0 MPa, the peak strain of limestone grouting stone bodies with 30 mm cracks increased from 7.53×10^{-3} to 9.65×10^{-3} , with an increase of 2.12×10^{-3} . The peak strain of limestone with 50 mm cracks increased from 3.95×10^{-3} to 6.25×10^{-3} and increased by 2.30×10^{-3} .

In conclusion, with the increase of tensile strength of cement stones, the strength and deformation of grouting stone bodies of limestone with small preformed cracks ($=10$) are almost not affected. The strength and deformation of limestone grouting stone bodies with larger prefabricated crack (>10) are greatly affected, and the strength and deformation of limestone grouting stone bodies are more affected by the tensile strength of grouting stone bodies bonding with longer prefabricated crack lengths. With the increase of the tensile strength of cement stones, the number and distribution range of secondary cracks of limestone grouting stone bodies increased. The strength and deformation of limestone grouting stone bodies with small preformed cracks ($=10$) are almost unaffected, while the strength of limestone grouting stone bodies with large preformed cracks (>10) is increased, indicating that grouting reinforcement can increase the integrity of limestone and weaken the concentration of stress and displacement around the cracks of the model.

4. Conclusions

- (1) After grouting the fractured limestone, the displacement concentration around the fracture decreases. Moreover, the longer the prefabricated crack length is, the more obvious the displacement concentration degree decreases after grouting. That is, the longer the prefabricated crack is, the better the grouting reinforcement effect is. The total input energy, elastic energy, and dissipative energy absorbed during the failure of limestone reinforced by grouting increased to some extent
- (2) The greater the stiffness of the cement stones, the more concentrated the distribution of fractures in grouting stone bodies, and the more likely it is to be destroyed from the position of limestone grouting stone bodies' precast cracks. The greater the stiffness of the cement stones, the smaller the overall strength of the limestone with prefabricated cracks. Limestone grouting stone bodies with a longer crack length are more affected by the stiffness of cement stones
- (3) The change of cement stone internal friction angle has little effect on the failure of limestone grouting stone bodies' rock mass. Under the same cohesion of cement stones, when the length of prefabricated cracks is small, the number of secondary cracks is large and the distribution range is large. The strength and deformation of limestone with large prefabricated cracks are greatly affected by cement stones' cohesion. And the longer the prefabricated crack length, the greater the influence of the cohesion of the cement stones on the strength and deformation of the limestone grouting stone bodies
- (4) With the increase of the tensile strength of the cement stones, the strength and deformation of the limestone grouting stone bodies with small prefabricated cracks are hardly affected. The strength and deformation of limestone grouting stone bodies with

large cracks are greatly affected, and the longer the prefabricated crack is, the greater the influence of the tangential strength of the cement stones on the strength and deformation of limestone grouting stone bodies. With the increase of the tensile strength of cement stones, the number and distribution range of secondary fractures of limestone grouting stone bodies with different lengths of prefabricated fractures increase. The strength and deformation of limestone with small prefabricated cracks are hardly affected by cement stones' tensile strength

Data Availability

The data used to support the findings of this study are included within the article.

Conflicts of Interest

The authors declare that they have no conflicts of interest.

Acknowledgments

The authors are grateful to the teachers and students from Shandong University of Science and Technology and the Qiuji Coal Mine, for their kindly assistance in the collection of core samples and other data. This research work is supported by the National Natural Science Foundation of China (Grant No. 51974172), Natural Science Foundation of Shandong Province (Grant No. ZR201911150152), Open Fund of State Key Laboratory of Coal Mining (2021-CMCU-KF015) and Clean Utilization and SDUST Research Fund (Grant No. 2018TDJH102).

References

- [1] S. C. Li, Z. Zheng, R. T. Liu, X. C. Wang, L. Z. Zhang, and H. B. Wang, "Analysis on fracture grouting mechanism considering grout-rock coupling effect," *Chinese Journal of Rock Mechanics and Engineering*, vol. 26, no. 4, pp. 812–820, 2017.
- [2] J. N. Xu, W. S. Zhu, and S. W. Bai, "Multi-crack rock mass mechanical character under the state of compression-shearing—constitutive model," *Rock and Soil Mechanics*, vol. 14, no. 4, pp. 1–15, 1993.
- [3] Y. F. Zeng, Q. Wu, S. Liu, Y. Zhai, H. Lian, and W. Zhang, "Evaluation of a coal seam roof water inrush: case study in the Wangjialing coal mine, China," *Mine Water and the Environment*, vol. 37, no. 1, pp. 174–184, 2018.
- [4] A. Usmani, G. Kannan, A. Nanda, and S. K. Jain, "Seepage behavior and grouting effects for large rock caverns," *International Journal of Geomechanics*, vol. 15, no. 3, article 06014023, 2014.
- [5] R. Liu, Z. Zheng, S. Li, and H.-l. Yang, "Mechanical properties of fractured rock mass with consideration of grouting reinforcement," *China Journal of Highway and Transport*, vol. 31, no. 10, pp. 284–291, 2018.
- [6] R. H. C. Wong and K. T. Chau, "Crack coalescence in a rock-like material containing two cracks," *International Journal of Rock Mechanics and Mining Sciences*, vol. 35, no. 2, pp. 147–164, 1998.

- [7] H. Lee and S. Jeon, "An experimental and numerical study of fracture coalescence in pre-cracked specimens under uniaxial compression," *International Journal of Solids and Structures*, vol. 48, no. 6, pp. 979–999, 2011.
- [8] A. B. Shemirani, H. Haeri, V. Sarfarazi, and A. Hedayat, "A review paper about experimental investigations on failure behaviour of non-persistent joint," *Geomechanics and Engineering*, vol. 13, no. 4, pp. 535–570, 2017.
- [9] J. Toraño, R. R. Díez, J. M. Rivas Cid, and M. M. C. Barciella, "FEM modeling of roadways driven in a fractured rock mass under a longwall influence," *Computers and Geotechnics*, vol. 29, no. 6, pp. 411–431, 2002.
- [10] J. P. Morris, M. B. Rubin, G. I. Block, and M. P. Bonner, "Simulations of fracture and fragmentation of geologic materials using combined FEM/DEM analysis," *International Journal of Impact Engineering*, vol. 33, no. 1–12, pp. 463–473, 2006.
- [11] M. Bahaaddini, G. Sharrock, and B. K. Hebblewhite, "Numerical investigation of the effect of joint geometrical parameters on the mechanical properties of a non-persistent jointed rock mass under uniaxial compression," *Computers and Geotechnics*, vol. 49, pp. 206–225, 2013.
- [12] X. Wang and L. Tian, "Mechanical and crack evolution characteristics of coal-rock under different fracture-hole conditions: a numerical study based on particle flow code," *Environment and Earth Science*, vol. 77, no. 8, p. 297, 2018.
- [13] N. Wu, Z. Liang, J. Zhou, and L. Zhang, "Energy evolution characteristics of coal specimens with preformed holes under uniaxial compression," *Geomechanics and Engineering*, vol. 20, no. 1, pp. 55–66, 2020.
- [14] Y. Mijia, "Mechanism of grout penetrating in stochastic fractured rock mass and its stability analysis after reinforcement," *Chinese Journal of Rock Mechanics and Engineering*, no. 4, p. 416, 2000, https://kns.cnki.net/kcms2/article/abstract?v=3uoqIhG8C44YLTlOAIiTRKgchrJ08w1e79zTD32bjb4zZjFIMBL9ziwifGDdj09Xe720cXfr4TU8lCQ2gxgSMnFYpJgm_13n&uniplatform=NZKPT.
- [15] Q. Liu, Y. Zhou, L. Chaobo, and J. Zhang, "Experimental study on mechanical properties of mudstone fracture before and after grouting," *Journal of Mining & Safety Engineering*, vol. 33, no. 3, pp. 509–514, 2016.
- [16] Z. Wang, W. Qin, and Z. Lijuan, "Experimental study on static and dynamic mechanical properties of cracked rock after grouting reinforcement," *Chinese Journal of Rock Mechanics and Engineering*, vol. 39, no. 12, pp. 2451–2459, 2020.
- [17] Z. Wang and L. Li, "Experimental study on bending fatigue behavior of grouting reinforced rock with fracture," *Chinese Journal of Rock Mechanics and Engineering*, vol. 37, no. 8, pp. 1823–1832, 2018.
- [18] Z. H. Zhao, H. Liu, X. J. Gao, and Y. H. Feng, "Meso-macro damage deterioration of weakly cemented red sandstone under the coupling effect of high-humidity and uniaxial loading," *Engineering Failure Analysis*, vol. 143, article 106911, 2023.
- [19] W. Yuan, X. Wang, and X. B. Wang, "Numerical investigation on effect of confining pressure on the dynamic deformation of sandstone," *European Journal of Environmental and Civil Engineering*, vol. 26, no. 9, pp. 3744–3761, 2022.
- [20] X. Wang, W. Yuan, Y. Yan, and X. Zhang, "Scale effect of mechanical properties of jointed rock mass: a numerical study based on particle flow code," *Geomechanics and Engineering*, vol. 21, no. 3, pp. 259–268, 2020.
- [21] Q. Zhang, X. Wang, L.-g. Tian, and D.-m. Huang, "Analysis of mechanical and acoustic emission characteristics of rock materials with double-hole defects based on particle flow code," *Shock and Vibration*, Article ID 7065029, 11 pages, 2018.
- [22] H. F. Lu, A. D. Cao, Q. S. Liu, H. Zhang, Y. X. Wu, and Z. C. Wei, "Experimental study on mechanical properties of grouting consolidating bodies with inner defects," *Chinese Journal of Rock Mechanics and Engineering*, vol. 39, no. 8, pp. 1560–1571, 2020.
- [23] J. Shen, B. Liu, J. Chen, Y. F. Li, and Y. Chen, "Experimental study on mechanical properties of diabase fracture-grouting mass," *Chinese Journal of Rock Mechanics and Engineering*, vol. 39, no. S1, pp. 2804–2817, 2020.
- [24] J. T. Chen, J. H. Zhao, S. C. Zhang, Y. Zhang, F. Yang, and M. Li, "An experimental and analytical re-search on the evolution of mining cracks in deep floor rock mass," *Pure and Applied Geophysics*, vol. 177, no. 11, pp. 5325–5348, 2020.
- [25] C. Pu, F. Liu, and Y. Chen, "The study on post-peak mechanical properties of non-penetrating rock-like specimen," *Journal of Experimental Mechanics*, vol. 35, no. 6, pp. 1121–1128, 2020.
- [26] The Professional Standard Compilation Group of People's Republic of China, SL264—2020, *Specifications for Rock Tests in Water Conservancy and Hydroelectric Engineering*, China Water & Power Press, Beijing, 2020.
- [27] X. Wang, Z. J. Wen, and Y. J. Jiang, "Time-space effect of stress field and damage evolution law of compressed coal-rock," *Geotechnical and Geological Engineering*, vol. 34, no. 6, pp. 1933–1940, 2016.
- [28] X. Wang, Z. J. Wen, Y. J. Jiang, and H. Huang, "Experimental study on mechanical and acoustic emission characteristics of rock-like material under non-uniformly distributed loads," *Rock Mechanics and Rock Engineering*, vol. 51, no. 3, pp. 729–745, 2018.
- [29] S. He, *Calibration Method and Sensitivity Analysis of Limestone Meso-Mechanical Parameters Based on Particle Flow*, Shandong University, Jinan, 2018.
- [30] J. Wang, *Study on Mechanical Characteristics and Energy Evolution of Marble under Three-Axis Unloading*, Kunming University of Science and Technology, Kunming, 2018.